Applied Surface Science 716 (2026) 164621

Contents lists available at ScienceDirect

Applied Surface Science

journal homepage: www.elsevier.com/locate/apsusc

Full Length Article

Dyadic Ru-based nanomaterials for visible light-driven photocatalytic hydrogen evolution

Gerard Martí [a], Marc Alique [a], Isidoro López [b], Laia Francàs [a], Roger Bofill [a], Olivier Schott [c], Garry S. Hanan [c], Álvaro Lozano-Roche [a], Nuria Romero [d,*], Karine Philippot [d], Antoni Llobet [e], Mirco Natali [f], Jordi García-Antón [a,*], Xavier Sala [a,*]

[a] Departament de Química, Unitat de Química Inorgànica, Universitat Autònoma de Barcelona 08193 Cerdanyola del Vallès, Barcelona, Spain
[b] Laboratoire Interdisciplinaire Carnot de Bourgogne ICB UMR 6303, Université Bourgogne Europe, CNRS, F-21000 Dijon, France
[c] Département de Chimie, Université de Montréal, Montréal, Québec H3C 3J7, Canada
[d] CNRS, LCC (Laboratoire de Chimie de Coordination), UPR8241, University of Toulouse, UPS, INPT, Toulouse Cedex 4 F-31077, France
[e] Institute of Chemical Research of Catalonia (ICIQ), Barcelona Institute of Science and Technology (BIST), Avda. Països Catalans, 16, 43007 Tarragona, Spain
[f] Department of Chemical, Pharmaceutical and Agricultural Sciences, University of Ferrara, Via L. Borsari 46, Ferrara 44121, Italy

ARTICLE INFO

Keywords:
Ruthenium nanoparticles
Organometallic approach
Hydrogen evolution reaction
Photocatalysis
Dyads
Hybrid nanomaterials

ABSTRACT

Visible light-driven water splitting is an appealing strategy to store renewable energy in the chemical bonds of molecular hydrogen. In this regard, the development of photocatalytic architectures where charge transfer and recombination can be controlled represents a key challenge. The surface functionalization of Ru/RuO_2 nanoparticles (NPs) with the $[Ru(2,2'\text{-bpy})_2(qpy)](PF_6)_2$ photosensitizer (PS), yielding PS-NPs "dyadic" hybrid nanomaterials, represents a promising strategy. Four HER photocatalysts with different PS:NPs ratios are synthesized and thoroughly characterized by analytical and spectroscopic techniques. X-ray photoelectron spectroscopy (XPS) reveals the covalent binding of the PS to the NPs surface. Analysis of the photocatalytic performance in aqueous triethanolamine (TEOA) shows that the activation of the nanocatalyst (RuO_2 reduction) and the hydrogen evolution rate improves when the PS loading increases. Under visible-light irradiation, the nanomaterials with higher PS loading show sustained production of hydrogen for at least 80 h. The morphological and compositional evolution of the hybrid nanomaterials under photocatalytic conditions is studied and correlated with hydrogen production rates over time, pointing to a sequential leaching of PS from the nanomaterials surface. Additionally, photophysical experiments allow attaining an insight into the photochemical mechanism, which involves oxidative quenching with a fast electron injection, but also fast back electron transfer.

1. Introduction

The continuous growth in global energy demand together with the impact of fossil fuels burning has urged the development of renewable, carbon-free energy conversion and storage strategies. Taking inspiration from nature, energy storage in chemical bonds has become a promising alternative [1]. In this regard, sunlight-driven bond formation for energy storage purposes was born under the name of artificial photosynthesis. Among the different approaches, water splitting is one of the most appealing ones [2–3], because water reduction yields molecular hydrogen, a zero-carbon molecule with high gravimetric energy density [4]. This green hydrogen can then be directly used as a fuel, converted to electricity *via* fuel-cell technology, or serve as a feedstock for other relevant chemical processes such as CO or CO_2 hydrogenation [4,5].

Even if the reduction of water to H_2 is not very energetically demanding ($E^0 = -0.41$ V vs. NHE at pH 7), its kinetics are usually slow, requiring the use of adequate catalysts [3]. It is well known that Pt is the benchmark metal for the hydrogen evolution reaction (HER) because of its balanced Pt-H binding energy, making it the metal of choice for many studies [6–8]. However, its high price makes it unsuitable for large scale applications. Moreover, Pt corrodes under alkaline conditions and shows limited water dissociation kinetics at neutral pH, which limits its applications only to acidic media. Recently, Ru-based nanomaterials have arisen as an alternative to Pt, showing low HER overpotentials and

* Corresponding authors.
E-mail addresses: nuria.romero@lcc-toulouse.fr (N. Romero), jordi.garciaanton@uab.es (J. García-Antón), xavier.sala@uab.cat (X. Sala).

https://doi.org/10.1016/j.apsusc.2025.164621
Received 14 June 2025; Received in revised form 25 August 2025; Accepted 12 September 2025
Available online 14 September 2025
0169-4332/Crown Copyright © 2025 Published by Elsevier B.V. This is an open access article under the CC BY-NC-ND license (http://creativecommons.org/licenses/by-nc-nd/4.0/).

sustained stability along the full pH range [9–11].

The design of photocatalytic materials for HER has led to two different approaches: electron-mediated systems and non-electron-mediated ones [12]. On the one hand, the use of electron mediators, such as TiO_2 or methyl viologen (MV^{2+}), allows better charge separation, providing longer lifetimes of the charge-separated states [13–15]. However, the electron transfer kinetics from the photosensitizer (PS) to the catalyst is slowed down by the presence of the mediator. On the other hand, non-electron-mediated systems allow direct electron injection to the catalyst, but charge recombination kinetics are much faster too [16]. In the case of molecular "dyadic" materials, composed of a molecular PS covalently bound to a molecular catalyst, photocatalytic HER has proven to be successful [17,18]. These photocatalysts, though, are barely soluble in water and require of organic solvents or aqueous/organic mixtures [17–20]. Moreover, the PS:catalyst ratio is usually limited, mostly due to the synthetic difficulties or limitations to integrate several bulky PS units in the coordination sphere of the metallic center [20,21]. In this regard, a promising alternative could be to use metallic NPs as catalytic species, which have been proven to be very active catalytic systems in electrocatalytic HER. Indeed, it is known that small metal NPs present a large surface area with numerous active sites that could lead to attachment of several PS molecules to a single NP and thus enhancing the electron flow to the catalytic sites. However, such systems have not been reported yet. The closest approach was proposed by Fukuzumi and co-workers, who studied the performance of a mixture made of suspended Ru NPs mixed with a donor–acceptor linked couple (2-phenyl-4-(1-naphthyl)-quinolinium ion, $QuPh^+$-NA, Fig. 1a) found in solution [6,22]. Efficient HER was achieved as the result of the $QuPh^+$-NA long-lived charge separated state. However, this donor–acceptor linked couple mainly absorbs in the UV range and needs organic solvents for its proper dissolution. Besides the $QuPh^+$-NA ion, the combination of NPs as catalysts with water-soluble PSs able to absorb in the visible range of the spectrum has relied on the use of electron transfer mediators, which take electrons from the excited PS entities and transfer them to the NPs [23,24]. These studies have revealed the importance of several parameters for the well-functioning of the overall photocatalytic systems [13,25–28].

In previous works, we have already pointed out the potential of the organometallic approach for the tailored synthesis of ligand-capped Ru NPs, a synthetic strategy based on the decomposition of a Ru precursor under 3 bar of H_2 in the presence of a ligand as stabilizing agent [9,29–31]. This method is highly reproducible and allows a fine control over the size, shape and surface composition of the prepared particles, together with easy fine-tuning of their properties for catalytic applications (*i.e.*, HER). Concretely, Ru NPs stabilized with 4-phenylpyridine (4PP, Fig. 1b) have shown excellent performance as a HER electrocatalyst, showing overpotentials at -10 mA·cm^{-2} as low as 20 mV, TOF values per active site of ca. 17 s^{-1} ($\eta = 100$ mV) and no sign of deactivation for at least 12 h when studied in 1.0 M H_2SO_4 [9]. The transfer of Ru-4PP NPs to dye-sensitized TiO_2-mediated photocatalytic systems has also been successful, revealing the importance of having an adequate PS-NPs connectivity for efficient electron transfer and, consequently, efficient HER [13].

Herein we report the first set of PS-NPs-based "dyadic" systems to attain visible-light driven hydrogen evolution in aqueous media without using electron mediator species. This approach is based on the synthesis of covalently bound PS-Ru NPs hybrid nanomaterials by organometallic methods [29]. $[Ru(2,2'\text{-bpy})_2(qpy)](PF_6)_2$ (2,2′-bpy: 2,2′-bipyridine; qpy: 4,4′:2′,2″:4″,4‴-quaterpyridine, Fig. 1c) was chosen as PS for two main reasons: i) from a coordination point of view, the dangling pyridines of the PS can bind to Ru NPs similarly to those in the 4PP ligand (Fig. 1b), shown to be an excellent electronic modulator when capping Ru NPs for electrocatalytic HER [9], and ii) from a photophysical perspective, the addition of the qpy ligand enhances the lifetime of the PS excited state (1.44 μs) compared to the classical $[Ru(2,2'\text{-bpy})_3]^{2+}$ (0.87 μs) [32]. Furthermore, the LUMO of the qpy-functionalized PS was found to be centered in the qpy ligand [32], thus possibly facilitating direct electron injection into Ru NPs upon visible-light irradiation. The $[Ru(2,2'\text{-bpy})_2(qpy)](PF_6)_2$ PS has already been combined with molecular catalysts in HER photocatalysis under blue-light irradiation (DMF, 1.0 M triethanolamine (TEOA), 0.1 M HBF_4 48 % in water), showing to remain stable for up to 4 h [32]. Following this track, four hybrid nanomaterials with different PS:Ru NPs ratios have been synthesized and tested using TEOA as the sacrificial electron donor (SED). Through exhaustive characterization, a detailed understanding of the PS loading on the Ru NPs and the relevance of the PS-NPs interaction is given, revealing some of the key parameters for the rational design and development of PS-NPs-based "dyadic" systems for photocatalytic HER.

2. Experimental section

2.1. Chemicals and reagents

All procedures involving the synthesis of ruthenium nanoparticles were carried out using tightly sealed Fischer-Porter vessels in the absence of oxygen, either in a Schlenk line or a glovebox. All glassware was washed with acid and properly rinsed and dried at 100 °C for several hours before each use. [Ru(COD)(COT)] (COD: 1,5-cyclooctadiene, COT: 1,3,5-cyclooctatriene) was acquired from NanoMePS. Ruthenium trichloride trihydrate was purchased from Johnson Matthey. Anhydrous dichloromethane (DCM), N,N-dimethylformamide (DMF), and diethyl ether were acquired from Scharlab. 2,2′-bipyridine (2,2′-bpy), ethylene glycol, 4,4′-bipyridine (4,4′-bpy), Pd 10 % on activated carbon, ammonium hexafluorophosphate and triethanolamine were purchased from Merck. Low molecular weight poly(methyl methacrylate) (PMMA) was purchased from BDH. Lithium chloride was purchased from Panreac. Deuterated solvents for NMR were purchased from Eurisotop. Tetrahydrofuran (THF) was distilled over sodium/benzofenone, hexane was

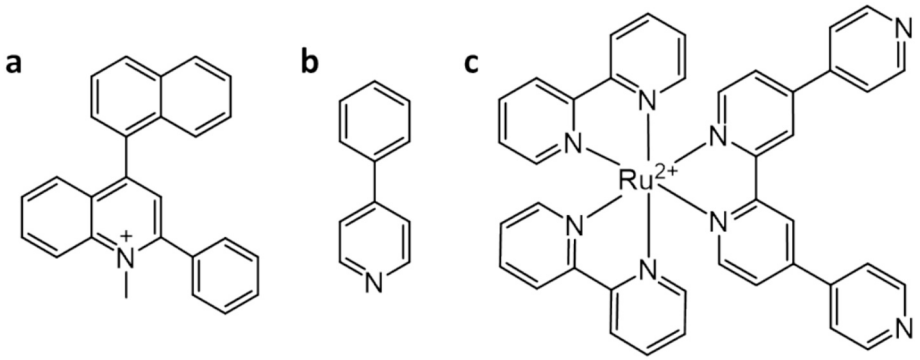

Fig. 1. Chemical structures of $QuPh^+$-NA (a), 4-phenylpyridine (4PP) ligand (b) and $[Ru(2,2'bpy)_2(qpy)](PF_6)_2$ (2,2′-bpy: 2,2′-bipyridine; qpy: 4,4′:2′,2″:4″,4‴-quaterpyridine) PS used in this work (c).

distilled over calcium hydride and methanol (MeOH) was distilled over magnesium in stills and kept under argon. THF and hexane were degassed by means of the freeze–pump–thaw methodology and MeOH was degassed by bubbling Ar for 20 min in a tightly closed Schlenk to assure the absence of oxygen in all solvents. 4,4′:2′,2″:4″,4‴-quaterpyridine (qpy) and cis-[Ru(2,2′-bpy)$_2$Cl$_2$] were synthesized following previously reported methods [33,34]. Ru NPs stabilized with 4PP (Ru-4PP) were synthesized following previously reported methods by our research group [9].

2.2. Synthesis of the [Ru(2,2′-bpy)$_2$(qpy)](PF$_6$)$_2$ (PS)

The PS was synthesized by adapting a previously described method for a similar trisbipyridine-based Ru complex [35]. Briefly, *cis*-[Ru(2,2′-bpy)$_2$Cl$_2$] (0.10 g) and qpy (74.2 mg) were dissolved in ethylene glycol (20.0 mL). The solution was refluxed for 1 h and let to cool down to room temperature. Then, an aqueous NH_4PF_6 solution was added dropwise to precipitate the PS, which was filtered and washed three times with cold water and three times with diethyl ether. Yield 56 %.

2.3. Synthesis of PS-functionalized Ru/RuO$_2$ NPs

Ru NPs were synthesized following similar methods as previous reports from our group [9,13]. The PS (9.7, 19.4, 29.1 or 38.9 mg depending on the number of equivalents) were dissolved in dried, degassed THF:MeOH (3:1 v/v. 30.0 mL) under inert conditions. The solution was transferred to a Fischer Porter containing [Ru(COD)(COT)] (30.0 mg), which was then submitted to a H_2 atmosphere (3 bars) for 16 h. Half of the solvent volume was evaporated, and hexane (15.0 mL) was added to induce the precipitation of the NPs. After filtering, the solid materials were further washed with THF:MeOH (1:5 v/v, 30.0 mL) until no orange coloration was observed in the supernatant, obtaining the four hybrid nanomaterials as black powders. The obtained materials were then slowly exposed to air by the diffusion of oxygen to an Ar-filled screw cap vial at ambient conditions for 28 days, yielding the corresponding PS-functionalized Ru/RuO_2 NPs "dyadic" systems.

2.4. Characterization

High-resolution transmission electron microscopy (HRTEM) was performed using a JEM-2011 microscope working at 200 kV at the "Servei de Microscòpia i Difracció de Raigs X" of the UAB. Samples were prepared by drop casting the suspended hybrid nanomaterials on carbon-coated copper grids. Atomic resolution high-angle annular dark-field scanning transmission electron microscopy (HAADF-STEM) imaging was acquired at 300 kV on a Thermo Fisher Scientific Spectra 300 (S) TEM equipped with double aberration correction. Prior to observation, samples were cleaned using a Gatan Solarus II plasma cleaner in an oxygen atmosphere for 4 cycles of 30 s at 10 W. Elemental analysis (EA) and inductively-coupled plasma-optical emission spectroscopy (ICP-OES) were performed at the "Servei d'Anàlisi Química" at the UAB on an Agilent 5900 system. X-ray photoelectron spectroscopy (XPS) analyses were carried out with a PHI QUANTES instrument using a monochromatic Al Kα source (hν = 1486.7 eV, power of 50 W). The base pressure during spectra acquisition was lower than $1{\cdot}10^{-9}$ mbar. A binding energy (BE) of 83.96 eV for the Au $4f_{7/2}$ line for metallic gold was used to calibrate the instrument. The powdered nanoparticulated samples were mounted on the sample holder using Scotch double-sized tape to prevent electrical connection between the samples and the spectrometer analyzer. The flood gun system of the spectrometer under standard conditions was used to neutralize the surface and avoid differential charging effects during measurements [36]. All the spectra were acquired using a 200 μm spot for the X-ray beam. A pass energy of 280 eV and an energy step of 1 eV were used to record the survey spectra while a pass energy of 55 eV and an energy step of 0.05 eV were used for to acquire core level spectra. Sample damage during measurement was checked by comparing initial fast scan XPS core level spectra with the corresponding long acquisition time spectra discussed in the manuscript. No sign of degradation was detected. Data treatment was carried out with CasaXPS Version 2.3.27PR1.5 [37]. All spectra were calibrated by stablishing at 685.75 eV the peak assigned to F from the PF_6^- anion in the F 1s core level spectra. Shirley background was used in all the core-level spectra. Mixing components based on Voight functions, LF line shape as implemented in CasaXPS, were used for fitting the different core level spectra. Fitting of the N 1s core spectra from the nanoparticulated samples was achieved by a combination of two components featuring the same value of FWHM and constrained for a separation of 1.28 eV as deduced from the fitting of the N 1s core spectrum from a sample containing the pure photosensitizer. A TRIFT V nanoToF II (Physical Electronics, Chanhassen (MN), US) armed with a 30 kV Bi-LMIG was employed for ToF-SIMS measurements. The same experimental conditions were used to record all mass spectra at room temperature. Mass spectra were measured in the "bunched" mode. The LMIG gun was adjusted to deliver Bi_3^{++} primary ions with a dc current of 12 nA over a 80 μm raster size. The mass range was set between 0 and 2000 uma and the number of recorded frames was controlled to avoid exceeding the static limit dose (dose $<10^{13}$ ions cm^{-2}). Charge compensation with a dual beam (15 eV e$^-$/10 eV Ar$^+$) system was used in all cases. The powder samples were pressed with a spatula on double-sided adhesive tape in order to prevent electric contact with the sample holder and thus differential charging effects. The ToF-DR software (Physical Electronics) was used for data processing. All positive polarity mass spectra, except for that of the after photocatalysis sample, were calibrated using the CH_3^+ (m/z = 15.0235), $C_2H_2^+$ (m/z = 26.0156) and Ru^+ (m/z = 101.9043) peaks. Calibration of the positive polarity mass spectrum from the sample after photocatalysis was carried by using the CH_3^+ (m/z = 15.0235), $C_2H_2^+$ (m/z = 26.0156) and $Si_2OC_5H_{15}^+$ (m/z = 147.0661) peaks. UV–vis spectra were acquired using a Jasco V-750 spectrophotometer. After catalysis, each suspension was centrifuged, and 200 μL of the supernatant were mixed with 800 μL of Milli-Q water. The diluted samples were placed in a quartz cell (10 mm light path) and the UV–vis spectra from 690 to 390 nm were recorded. PS quantification was done by fitting the experimental data to a Rayleigh scattering baseline, as described in Eq. (1) [38], plus the signal coming from the PS (Fig. S18). The absorbance at 470 nm from the PS fitting signal was taken to do all related calculations and quantifications (Fig. S18). PS absorption was calibrated by measuring the absorbance at 470 nm at different PS concentrations (56.6, 42.5, 28.3, 14.2 and 3.5 μM in aqueous TEOA 2 % v/v, Fig. S19).

$$A_{Rayleigh} = A_0 + \log\left(\frac{1}{1 - c{\cdot}\lambda^{-4}}\right) \quad (1)$$

2.5. Photocatalytic experiments

Hydrogen evolving from photocatalytic experiments was measured by a Clark hydrogen electrode (Unisense H2-NPLR). The reaction was carried out in a thermostatic (25 °C) 7.2 mL cylindrical glass cell containing ca. 1.4 mg of the photocatalyst dispersed in the dark (5 min. in ultrasonic bath) and 5 mL of aqueous TEOA 10 % v/v as SED, with constant magnetic stirring. The tip of the Clark electrode was introduced into the cell headspace (Fig. S8), which was sealed with a septum and grease. The solution was Ar-bubbled for 15 min until the signal of the Clark electrode stabilize for a minimum of 2 min. Then, an Abet 10 500 solar simulator bearing a Xe lamp and placed at 1 Sun (100 mW cm^2) distance was used to irradiate the sample. The lamp-cell distance was calibrated using a photodiode connected to a multimeter, which allowed to determine the light irradiation by measuring the current intensity generated. After each photocatalytic experiment, where the maximum H_2 volume generated has been 34 μL, the cell was Ar-bubbled and calibrated by the injection (gastight Hamilton syringe) of known H_2 volumes (10, 20, 30 and 40 μL, Fig. S11).

Ru-4PP was used as a reference blank system and the physical mixture of Ru-4PP (0.25 mg) and PS (0.90 mg) was tested as a representative non-bonded system, being the proportion of Ru NPs to PS the same as in **RuPS-0.4**.

2.6. Photophysical experiments

A Cary 300 UV–Vis spectrometer (Agilent Technologies) and an Edinburgh FLS 920 spectrofluorometer were employed to record the absorption and emission spectra, respectively., A custom laser spectrometer including a Continuum Surelite II Nd:YAG laser (FWHM 6–8 ns) bearing the option of frequency tripling (355 nm) and a Xe light source (Applied Photophysics) comprising a model 720 (150 W) lamp housing, a model 620 power-controlled lamp source and a model 03–102 arc lamp pulser were used for time-resolved emission and absorption measurements. Laser excitation was run at 90° with respect to the white light probe beam. A 300 mm focal length Acton SpectraPro 2300i triple grating, flat field, and double exit monochromator equipped with a photomultiplier detector (Hamamatsu R3896) was used to process the light emitted or transmitted by the sample. A Teledyne LeCroy 604Zi (400 MHz, 20 GS s^{-1}) digital oscilloscope was used to process the signals from the photomultiplier. Diverging lens were used to defocue the excitation pulse (355 nm wavelength) and set to an average energy of ~5 mJ/pulse by means of a combined neutral density filters acquired from Edmund Optics. All solutions were purged with a constant N_2 flow for 15 min and were kept sealed before each measurement, avoiding interference due to the presence of molecular oxygen. Solid samples were prepared by either dissolving the PS or suspending the NPs in a 20 mg/mL poly(methyl methacrylate) (PMMA) solution in dichloromethane. The solution was then put in a watch glass and left to dry at room temperature, obtaining thin films containing the materials.

3. Results and discussion

3.1. Synthesis and characterization of PS-Ru NPs hybrid nanomaterials

The hybrid nanomaterials were synthesized by the organometallic approach followed by a controlled passivation of the Ru NPs surface (Fig. 2), similarly to our previously reported works [9,13]. The PS-functionalized Ru NPs were obtained by reduction with hydrogen (3 bar) of [Ru(COD)(COT)] (COD: 1,5-cyclooctadiene; COT: 1,3,5-cyclooctatriene) in THF:MeOH (3:1 v/v), using $[Ru(2,2'\text{-bpy})_2(qpy)](PF_6)_2$ as both the stabilizer during the synthetic procedure and then as the PS during photocatalysis (Fig. 2). The [PS]/[Ru] ratio varied from 0.1 to 0.4 molar equivalents, thus aiming at four different hybrid nanomaterials: **RuPS-0.1**, **RuPS-0.2**, **RuPS-0.3** and **RuPS-0.4**. Then, the precipitation of NPs was induced by the addition of hexane, and the hybrid nanomaterials were further washed with THF:MeOH (5:1 v/v) until no orange coloration of the supernatant (due to the unbound PS) was observed. The obtained hybrid nanomaterials were dried under vacuum and then exposed to air by slow oxygen diffusion at ambient conditions into a screwed cap vial. Such mild conditions (Fig. 2) prevent fast oxidation of the Ru NPs and allow a controlled passivation of the hybrid nanomaterial, ensuring the preservation of the initial structure in the final Ru/RuO_2 NPs. [9].

The obtained hybrid nanomaterials were characterized using multiple techniques. High resolution transmission electron microscopy (HRTEM) characterization showed that all hybrid nanomaterials were made of small, similarly sized NPs (1.1–1.3 nm mean size) with narrow size distribution (Fig. 3a–d, Fig. S1). However, aggregates of NPs were also observed whose formation can result from interaction between the ligands of the PS (like π-π stacking) [39]. High-angle annular dark field-scanning transmission electron microscopy (HAADF-STEM) exposed the presence of interplanar distances corresponding to both Ru and RuO_2 phases in the NPs (Fig. 3a–d), as expected from the slow passivation process [30]. Moreover, bright dots were observed close to the Ru/RuO_2 NPs surface (Fig. 3e, Fig. S2), which were attributed to Ru(II) metallic centers of the nearby PS complexes. In addition, energy dispersive X-ray spectroscopy (EDX) mapping (Fig. S3) showed the presence of nitrogen, phosphorous and oxygen in the Ru-rich areas, corroborating both the partial oxidation of Ru to RuO_2 and the successful surface-functionalization of the NPs with the PS. Elemental analysis (EA) allowed the determination of the PS loading through the nitrogen content of the hybrid nanomaterials (Fig. S4, Table S1, Table S2). It was determined that **RuPS-0.1** contained 31 % (w/w) of PS, **RuPS-0.2** 43 %, **RuPS-0.3** 53 % and **RuPS-0.4** 64 %. As expected, when increasing the [PS]/[Ru] molar ratio in the synthesis, the final PS loading in the hybrid nanomaterials also increased. Combining EA with ICP-OES data (Table S2), the Ru content into the Ru/RuO_2 NPs was determined to be 39 % (w/w) for **RuPS-0.1**, 27 % for **RuPS-0.2**, 21 % for **RuPS-0.3** and 14 % for **RuPS-0.4** (Fig. S4). From these data, if we calculate the number of PS equivalents per superficial Ru site using the magic number rule, we get PS molecules/surface Ru atom values of 0.11, 0.23, 0.34 and 0.60 and PS molecules/RuNP values of 7, 14, 17 and 24 (Table S2). Given the bulkiness of the PS, these ratios are high and very unlikely to fit at the NPs first coordination sphere (see Table S2), suggesting that part of the PS molecules could be in a second shell, weakly interacting with the Ru NPs surface (*i.e. via π*-stacking). The composition of the hybrid nanomaterials was analyzed by X-ray photoelectron spectroscopy (XPS). The Ru $3p_{3/2}$ core-level spectra exhibited a peak centered at 462.3 eV across all four samples (Fig. 4a and Fig. S5). This value lies between the binding energy observed for anhydrous RuO_2 (462.6 eV) and those recorded for the PS (461.9 eV) and metallic Ru (461.3 eV). These findings suggest that the nanoparticles comprise a mixture of oxidation states: Ru(II), originating from PS in the shell, as well as Ru(0) and Ru(IV), present in the core. Decomposition of the N 1s core-level spectra of the hybrid nanomaterials indicated that part of the dangling pyridines of the PS were indeed coordinated to Ru atoms from the Ru/RuO_2 NPs. Compared to the free PS (Fig. 4c), the relative area of the N 1s component at 398.3 eV corresponding to uncoordinated N atoms decreased in all hybrid nanomaterials (Fig. 4d, Fig. S6), thus proving the PS-NPs interaction [40]. Finally, time of flight-secondary ion mass spectrometry (ToF-SIMS) analysis of the hybrid nanomaterials showed the same peak fragment distribution as the free PS (Fig. S7), proving the integrity of the PS at the NPs surface and ruling out the partial hydrogenation of the qpy and 2,2′-bpy ligands of the PS under the used reductive synthetic conditions (3 bar H_2).

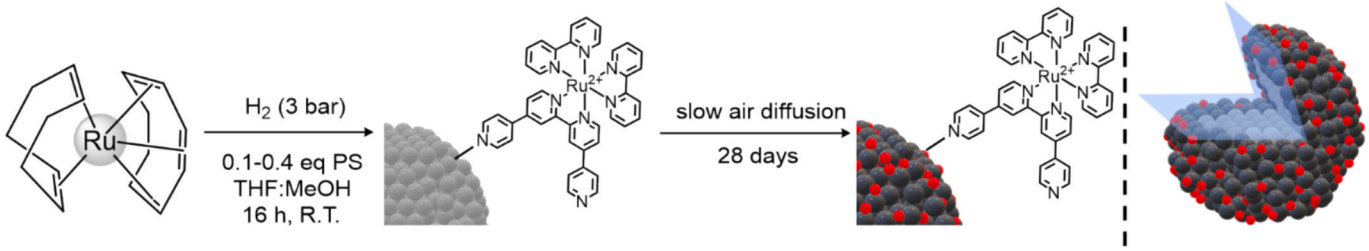

Fig. 2. Synthesis of PS-functionalized Ru/RuO_2 NPs "dyadic" nanomaterials (right) and section of a Ru/RuO_2 NP (left).

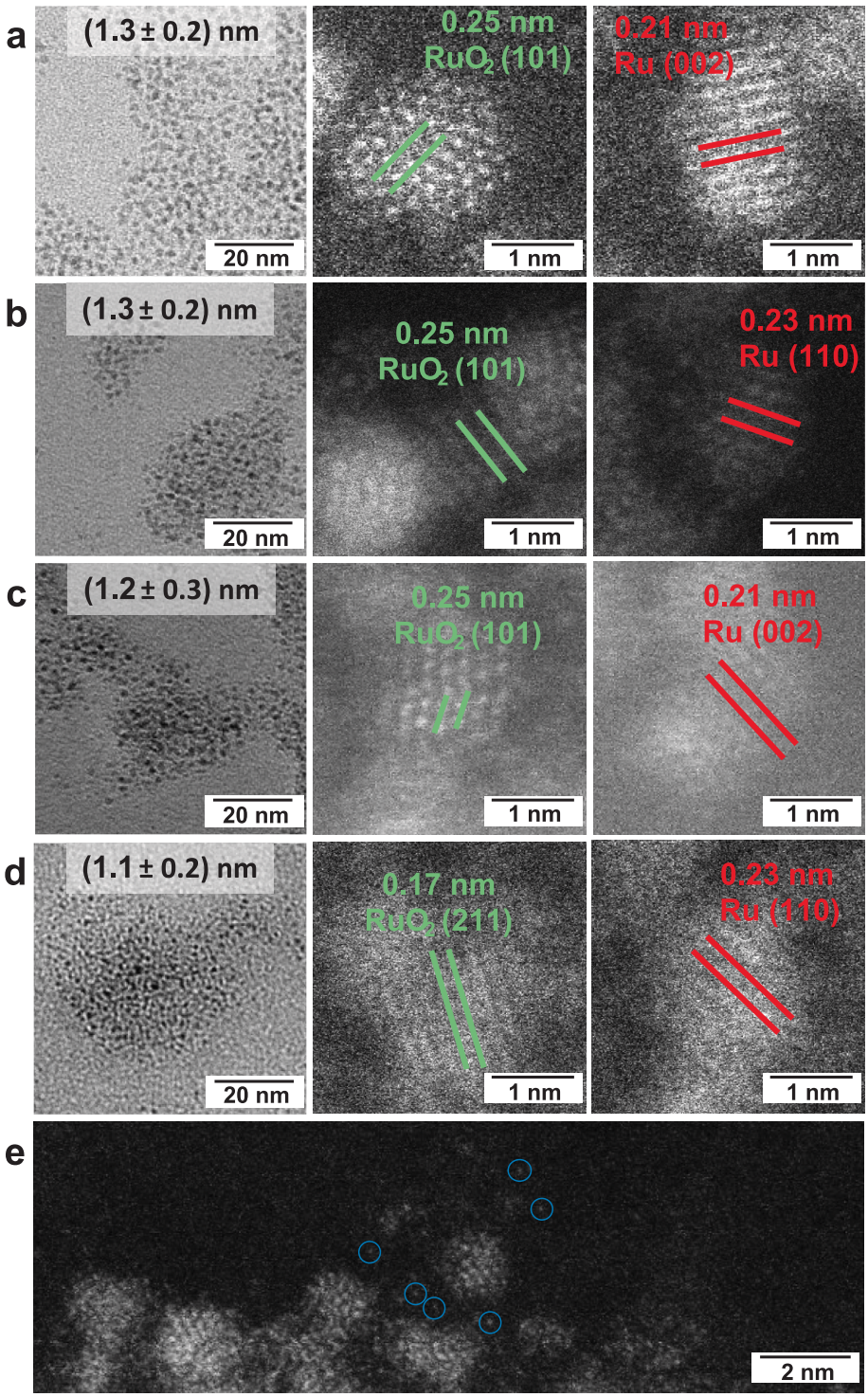

Fig. 3. High-resolution TEM with particle mean sizes and HAADF-STEM images showing Ru (Ru(0)) and RuO_2 (Ru(IV)) phases of **RuPS-0.1** (a), **RuPS-0.2** (b), **RuPS-0.3** (c) and **RuPS-0.4** (d) hybrid nanomaterials. HAADF-STEM image of **RuPS-0.3** (e) showing the bright dots observed around the Ru/RuO_2 NPs (circled in blue), which correspond to Ru(II) metallic centers of PS complexes around the NPs surface.

3.2. Photocatalytic HER studies

The photocatalytic HER performance of the four hybrid nanomaterials under visible-light illumination ($\lambda > 400$ nm) calibrated to 1 Sun of intensity was evaluated in aqueous TEOA 10 % v/v as SED at 25 °C (Figs. S8 and S9) [13]. The results are summarized in Table 1.

The four hybrid nanomaterials did not show hydrogen release from the very beginning of irradiation. Indeed, the production of hydrogen was observed after an induction time, which was found to be different for each hybrid nanomaterial, which could be attributed to the reduction of the RuO_2 outer shell of the NPs to Ru(0). In electrocatalytic HER, RuO_2 is known to be reduced to Ru(0), which is the actual catalytically active species [9,30]. **RuPS-0.1** showed no hydrogen evolution up to 72 h of visible-light illumination (Table 1, entry 1). The other hybrid nanomaterials showed induction times that decreased as the PS loading increased (Table 1, entries 2–4), suggesting a relationship between these

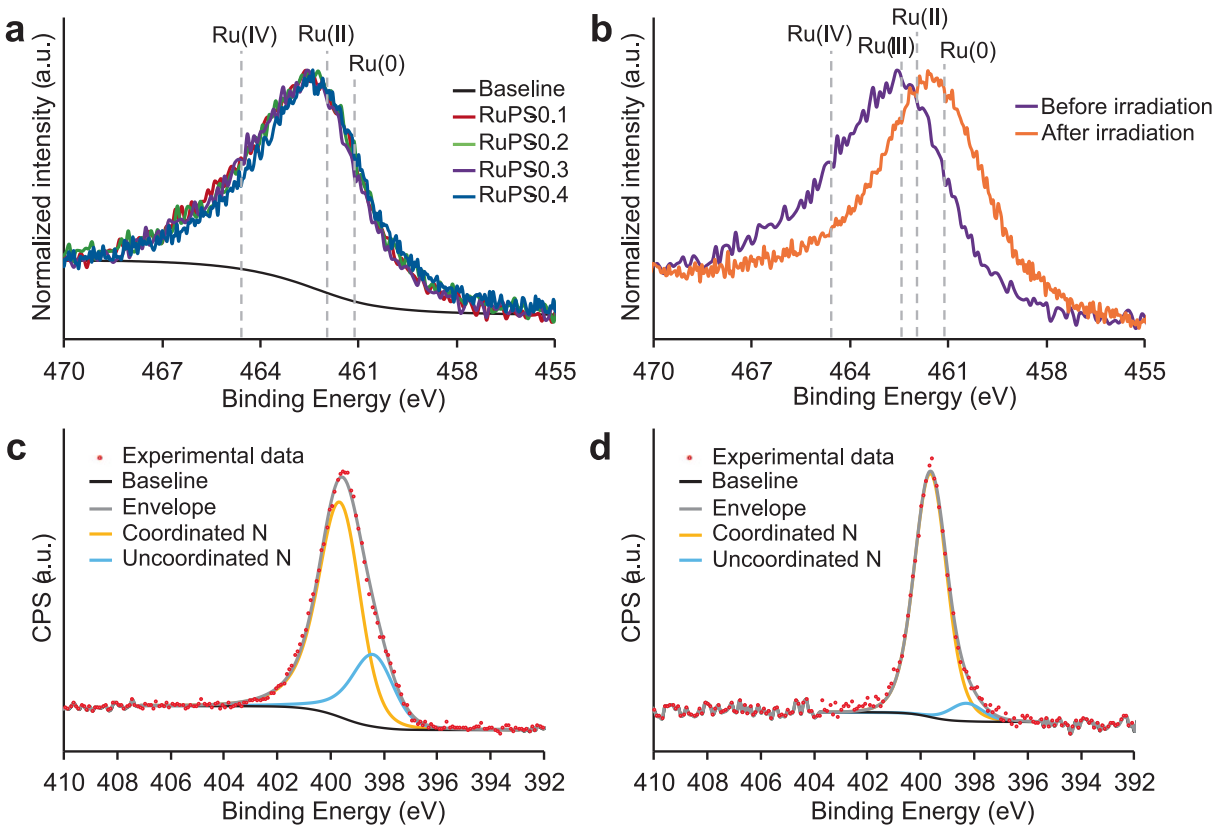

Fig. 4. XPS Ru $3p_{3/2}$ core-level spectra of the four hybrid nanomaterials (a) and of **RuPS-0.3** before and after visible light illumination for 70 h (20 mg in 5 mL aqueous TEOA 10 % v/v) (b). XPS N 1s core-level spectra of the free PS (c) and of **RuPS-0.3** hybrid nanomaterial (d) showing the signal decomposition into coordinated (399.6 eV) and uncoordinated (398.3 eV) nitrogen.

Table 1
Visible light driven (1 sun, $\lambda > 400$ nm) H_2 evolution performance of the four hybrid materials (1.3–1.5 mg) in aqueous TEOA 10 % *v/v* (5 mL) at 25 °C.

Entry	Hybrid nanomaterial	PS loading [% w/w]	Induction time [h]	Hydrogen evolution rate [μmol h^{-1} g_{Ru}^{-1}][b]	Maximum Hydrogen evolution rate [μmol h^{-1} $g_{material}^{-1}$]	Maximum Hydrogen evolution rate [μmol h^{-1} $g_{Rusurface}^{-1}$]
1	**RuPS-0.1**	31	–[a]	–[a]	–[a]	–[a]
2	**RuPS-0.2**	43	30.0 ± 0.5	1.8 ± 0.4	0.5 ± 0.1	2.4 ± 0.5
3	**RuPS-0.3**	53	14.9 ± 0.4	47.4 ± 4.6	9.8 ± 0.9	63.2 ± 6.1
4	**RuPS-0.4**	64	8.1 ± 0.4	74.9 ± 13.7/29.8 ± 3.1[c]	10.2 ± 1.8	96.0 ± 15.9

[a] This material did not show any hydrogen production after 72 h under visible-light illumination.
[b] H_2 evolution rate after 30 h (counted after the induction time) of hydrogen evolution. g_{Ru} refers to grams of Ru from the NPs only.
[c] A decrease of the hydrogen evolution rate was observed after ca. 10 h under visible-light illumination, reaching a stable rate of 37.9 μmol h^{-1} g_{Ru}^{-1} after 30 h under turnover conditions.

two parameters. To shed some light on such a correlation, the reduction of the Ru/RuO_2 NPs surface was studied by XPS using a concentrated suspension of **RuPS-0.3** (4 mg mL^{-1}) in aqueous TEOA 10 % *v/v* exposed to irradiation. The Ru $3p_{3/2}$ XPS signal of the **RuPS-0.3** hybrid nanomaterial after irradiation showed a clear shift (0.9–1.1 eV) towards lower binding energies compared to the initial state (Fig. 4b). This shift arises from the reduction of Ru(IV) from RuO_2 to Ru(0), indicating that an activation of the hybrid nanomaterials happens under photocatalytic conditions. During the irradiation time some Ru(III) species can be formed due to the formation of oxidized PS species (PS^+) [41]. This way, the difference in induction times observed between the hybrid nanomaterials may depend on how fast the reduction of the RuO_2 shell of the NPs occurs. On the basis of this hypothesis, the **RuPS-0.3** hybrid nanomaterial, which has one of the highest PS loadings (and thus one of the highest incoming electron flow) can be expected to be reduced more rapidly and promptly for H_2 production, as experimentally observed. The hydrogen evolution rates of the hybrid nanomaterials under visible-light irradiation could be evaluated after 30 h of hydrogen evolution (counted after each corresponding induction time), except for **RuPS-0.1**, where no hydrogen was detected after 72 h irradiation. The results showed that the higher the PS loading, the higher the hydrogen evolution rate observed (Table 1, entries 2–4; Fig. S9), and that when the PS and the Ru NPs were physically mixed (not connected by a chemical bond) no hydrogen was evolved (Fig. S10). As for the induction time above, this trend can also be explained by the higher incoming electron flux expected at higher PS loadings. Interestingly, **RuPS-0.3** and **RuPS-0.4** showed a 43 and 39-fold increase in the normalized (per Ru weight on the NPs) H_2 production after 30 h of photocatalysis, respectively, compared to **RuPS-0.2** (Fig. S9). Moreover, **RuPS-0.4** showed a decrease in the H_2 evolution rate after ca. 10 h, the resulting slope resembling the one of **RuPS-0.3** (Table 1, entries 3 and 4; Fig. S9). This decrease in activity suggests an evolution of the hybrid nanomaterial under photocatalytic turnover. In order to shed light to this decrease of activity, both solid and liquid fractions were collected after

photocatalysis for the four hybrid nanomaterials and analyzed by HRTEM and UV–Vis spectroscopy. HRTEM images of the solid fractions showed no significant changes in size, morphology or aggregation state of the NPs, which resembled those of the as synthesized materials (Fig. S12). However, UV–Vis spectra of the solutions evidenced the presence of PS in the aqueous phase, indicating its partial release from the hybrid nanomaterials during the photocatalytic experiments (Fig. S13). This release was determined to be more significant at higher PS loadings. A monitoring of the hydrogen evolution along the reaction time for the most active samples, **RuPS-0.3** and **RuPS-0.4**, allowed us to get insight between the decrease of activity and PS release (Fig. 5). The results show two regimes (see the evolution of black dots in Fig. 5a and Fig. 5b, respectively): i) a fast PS detachment happening at the beginning of the photocatalytic experiment ($t < 20$ h, red ovals in Fig. 5), and ii) slower PS detachment taking place after several hours (from ca. 20 h onwards, blue ovals in Fig. 5) under turnover conditions. Such a PS detachment can be linked to previous work by Philippot and co-workers where Ru molecular complexes were shown to form outer and inner layers when employed as stabilizers on Ru/RuO_2 NPs [39]. Thus, the molecular complex molecules directly coordinate to the Ru/RuO_2 NPs surface in the inner layer, while electrostatic forces allow to keep extra complex molecules in an outer layer around the Ru/RuO_2 core. We can therefore make the hypothesis that the PS in our systems stands around the Ru/RuO_2 NPs in different layers, with an outer layer where the PS easily detaches from the NPs surface (fast detachment regime, red ovals in Fig. 5), and an inner layer where the PS is more strongly engaged with the NPs surface (slow detachment regime, blue ovals in Fig. 5). In the case of **RuPS-0.3**, the fast PS detachment process finishes just when catalysis starts (Fig. 5a), showing constant HER activity afterwards. On the contrary, **RuPS-0.4** already starts evolving hydrogen during the fast detachment process (Fig. 5b). Thus, when the fast release of PS ends, a decrease in the HER rate of the hybrid nanomaterial occurs, in line with the complete loss of the outer PS layer (Fig. 5b The stability of the hybrid nanomaterial at long photocatalysis times was studied for **RuPS-0.3**, which was capable of evolving hydrogen at a constant rate for ca. 80 h (Fig. S14), when it started to slowly deactivate. As shown in Fig. S15, HRTEM analysis of the solid fraction recovered after ca. 160 h under photocatalytic conditions showed well-defined NPs of similar size and morphology than those of the as synthesized **RuPS-0.3** hybrid nanomaterial. Deactivation is thus attributed to the amount of PS loss (ca. 85–90 %, Fig. S14, black dots). Even so, it is worth mentioning the photostability of the $[Ru(2,2'\text{-bpy})_2(qpy)](PF_6)_2$ PS both within the hybrid nanomaterials of this work (up to 120 h, Fig. S14) and in TEOA aqueous solution (after leaching from the Ru/RuO_2 NPs surface, Fig. S16), compared to its fast (ca. 4 h) photobleaching in acidified organic solution (under blue light irradiation) reported by Hanan and co-workers [32]. Further comparison of the photocatalytic activity and stability of the hybrid nanomaterials of this work with that of similar assemblies found in literature is presented in Table S3.

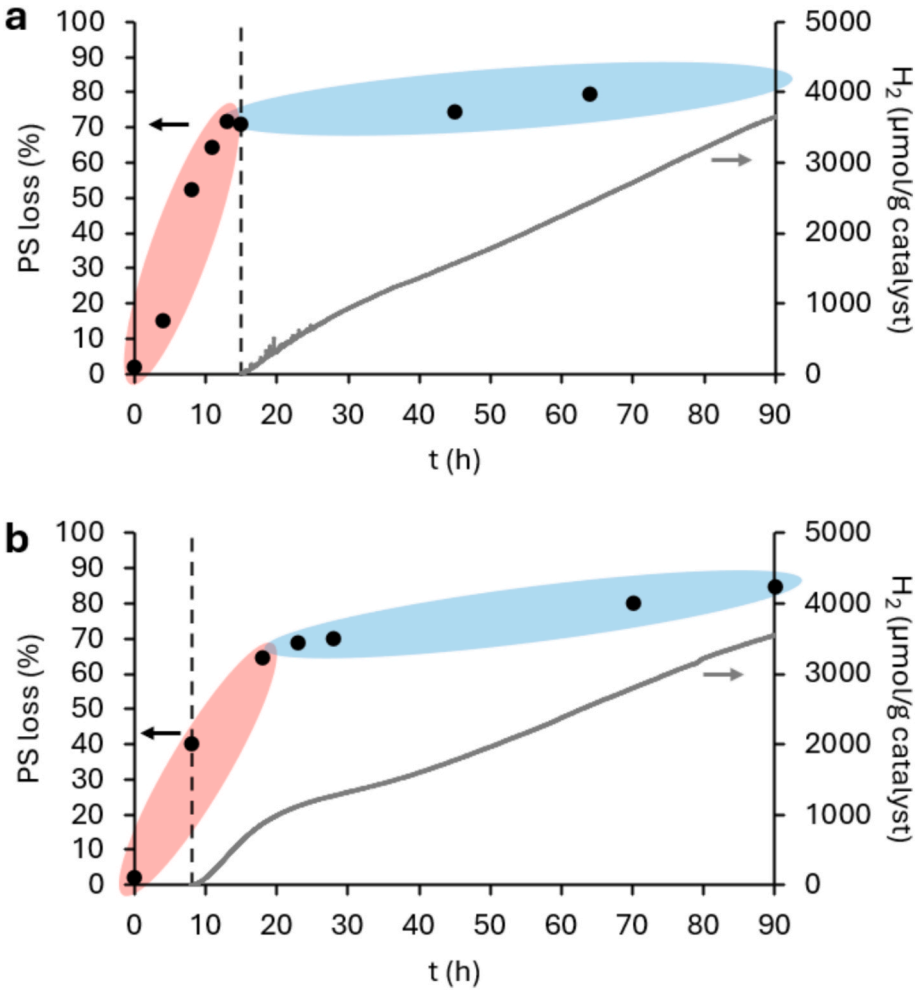

Fig. 5. Monitoring of hydrogen evolution and PS loss for **RuPS-0.3** (a) and **RuPS-0.4** (b) under photocatalytic conditions (1.3–1.5 mg of photocatalyst in 5 mL of aqueous TEOA 10 % v/v at 25 °C, 1 Sun, $\lambda > 400$ nm). Colored ovals represent fast (red) and slow (blue) PS detachment regimes. Dashed lines indicate induction times in each case. Grey solid lines indicate hydrogen evolution.

3.3. Photophysical studies

A photophysical analysis was performed aiming to shine light on the mechanistic aspects associated with the photogeneration of H_2 by the prepared hybrid nanomaterials. In this regard, H_2 formation upon photoirradiation can, in principle, occur either through an oxidative or a reductive quenching route [42,43]. In the former, excitation would involve an oxidative quenching of the PS by the Ru/RuO_2 NP as the primary photochemical process, followed by hole transfer to the sacrificial reagent. In the second option, excitation would lead to a reductive quenching of the PS by the sacrificial electron donor and a subsequent electron transfer from the reduced PS to the catalytic unit.

We first investigated the feasibility of a reductive quenching pathway by monitoring the luminescence of PS in the absence and in the presence of the sacrificial reagent. Remarkably, no change in the emission yield can be appreciated upon increasing the concentration of TEOA from 0 to 13.5 % v/v (Fig. S20). These results confirm that a reductive quenching mechanism cannot be operative in the present photocatalytic system. Thus, the photochemical reaction must proceed through an oxidative quenching route (Fig. 6), involving transfer of an electron from the excited PS* to the Ru/RuO_2 NP as the first photochemical event.

Time-resolved luminescence experiments (excitation at 355 nm) on the PS and the hybrid nanomaterials both in purely aqueous solution and in the presence of TEOA were performed to attain a deeper insight into this process. The kinetic traces are collected in Fig. S21. In all cases the decay can be well fitted to a single exponential, with the resulting lifetime being consistent with the one of the free PS* in aqueous solution. Similar results were also obtained by fixing the PS and **RuPS-0.3** in a PMMA matrix (Fig. S22). These results indicate that i) the observed emission decay in the hybrid nanomaterials is solely related to residual free PS and ii) the lifetime of the PS bound to the Ru/RuO_2 NPs has to fall below the time resolution of the laser flash photolysis apparatus (< 10 ns). These findings thus support a very fast electron transfer from the excited PS* to the Ru/RuO_2 NPs (Fig. 6).

Finally, transient absorption measurements were attempted in order to extract information on the possible photoproducts formed upon oxidative quenching. No detectable signals were recorded (see, e.g., the kinetic trace at 450 nm potentially associated with the oxidized PS^+ species, Fig. S23). This evidence thus suggests that both electron injection and back electron transfer are taking place at very short timescales (< 10 ns). In this respect, fast charge recombination phenomena can be consistent with the observation of loading-dependent induction time in the photocatalytic hydrogen evolution experiments (see above).

4. Conclusions

In summary, this work reports the first organometallic synthesis of PS-NPs "dyadic" photocatalysts for HER. The developed surface-functionalization strategy allows the fine control over the loading of the molecular PS on the Ru/RuO_2 NPs surface, which significantly influences the photocatalytic HER performance of the resulting hybrid nanomaterials. Thus, as the PS loading increases (and so does the corresponding flow of electrons arising from its excitation with visible light) the induction time for the catalysis to start (ascribed to surface RuO_2 reduction to metallic Ru) decreases and the hydrogen evolution rate increases. Characterization of the hybrid nanomaterials after photocatalysis showed no significant changes in size or morphology but certain leaching of the PS to the TEOA aqueous solution at long timescales. Correlation of the amount of PS leaching with the kinetics of H_2 production pointed out the existence of different PS layers around Ru/RuO_2: i) an inner layer where the PS molecular complexes are strongly engaged with the NPs surface, making the PS less prompt to detach, and ii) an outer layer where the PS is weakly interacting with the inner layer, making it easy for these PS molecular complexes to leach to the TEOA solution. Moreover, the photostability of the PS both in aqueous TEOA solution and when interacting with the Ru-based NPs in the hybrid nanomaterials reported in this work was found to be significantly enhanced when compared to its fast photobleaching when studied in an acidified organic solution [32]. Finally, photophysical characterization afforded insight into the photochemical mechanism, which involves an oxidative quenching with a fast electron injection, favorable towards catalyst activation, but also enabling a fast back electron transfer process. Thus, the observed variation in performance (H_2 production kinetics and long-term stability) according to the PS content and its binding mode to the Ru-based NPs points out the relevance of designing adequate PS-NP interactions for efficient HER photocatalysis. This work highlights the potential of NP surface-functionalization for the development of tunable NPs-based "dyadic" systems with molecular PSs, opening new ways for the rational design of HER photocatalysts. However, our results also reveal main challenges towards the practical application in HER of these systems. Minimizing charge recombination between the two components and stabilizing high concentrations of the PS at the NP surface appear as key factors to ensure fast and efficient H_2 evolution under photoirradiation. Strategies such as the polymerization of attachable PS moieties [44,45] (potentially increasing both the stability and the concentration of the PS at the NP surface) and the modulation of the PS conjugation by the introduction of alkylic linkers between the PS core and the anchoring groups [46,47] could be of interest to overcome these challenges.

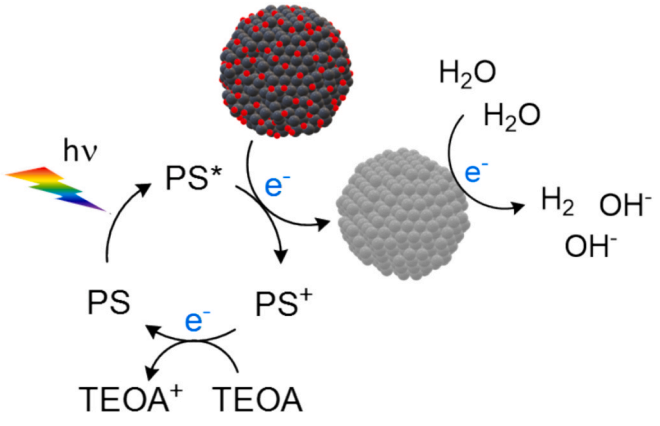

Fig. 6. Proposed photocatalytic cycle for the studied hybrid nanomaterials through oxidative quenching of the PS.

CRediT authorship contribution statement

Gerard Martí: Writing – review & editing, Writing – original draft, Supervision, Investigation, Formal analysis, Data curation. **Marc Alique:** Investigation. **Isidoro López:** Writing – review & editing, Resources, Investigation, Formal analysis, Data curation. **Laia Francàs:** Writing – review & editing, Supervision. **Roger Bofill:** Writing – original draft, Supervision, Data curation. **Olivier Schott:** Investigation. **Garry S. Hanan:** Writing – review & editing, Supervision, Resources, Funding acquisition. **Álvaro Lozano-Roche:** Investigation. **Nuria Romero:** Writing – review & editing, Supervision, Resources, Investigation, Conceptualization. **Karine Philippot:** Writing – original draft, Supervision, Funding acquisition. **Antoni Llobet:** Writing – review & editing, Supervision, Resources, Funding acquisition. **Mirco Natali:** Writing – review & editing, Writing – original draft, Resources, Investigation, Formal analysis, Data curation. **Jordi García-Antón:** Writing – review & editing, Writing – original draft, Supervision, Resources, Funding acquisition, Conceptualization. **Xavier Sala:** Writing – original draft, Supervision, Resources, Project administration, Conceptualization.

Declaration of competing interest

The authors declare that they have no known competing financial

interests or personal relationships that could have appeared to influence the work reported in this paper.

Acknowledgements

G.M. thanks the MICIU for the FPU predoctoral grant (FPU19/04322). L.F. thanks the RyC Fellowship (RYC2018-025394-I) and PID project (PID2021-128197NA-I00) funded by MCIN/AEI/10.13039/501100011033/FEDER. X.S. and J.G.-A. thank MINECO/FEDER (PID2019-104171RB-I00) and MICIU (PID2023-146787OB-I00) for financial support. AGAUR is gratefully acknowledged for financial support (CLIMA2023-00036). M.N. acknowledges the University of Ferrara for funding (FAR2024). I.L. acknowledges the Region Bourgogne Franche-Comté council through the "ELECTRICALLY" ANER project (2024PRE00037). Authors acknowledge the use of instrumentation as well as the technical advice provided by the Joint Electron Microscopy Center at ALBA (JEMCA) and funding from Grant IU16-014206 (METCAM-FIB) to ICN2 funded by the European Union through the European Regional Development Fund (ERDF), with the support of the Ministry of Research and Universities, Generalitat de Catalunya. A.L. thanks CERCA Program / Generalitat de Catalunya, and Severo Ochoa Excellence Accreditation CEX2024-001469-S funded by MCIU / AEI / 10.13039/501100011033, MICINN for PID2022-140143OB-I00 and Generalitat de Catalunya for the project 2021 SGR 01583.

Appendix A. Supplementary data

Supplementary data (Microscopy images, ICP-OES data, EA data, XPS data, ToF-SIMS data, H_2 evolution data, PS loss determination data, emission data, time-resolved luminescence data, transient absorption data, calculations and relevant related literature data.) to this article can be found online at https://doi.org/10.1016/j.apsusc.2025.164621.

Data availability

Data will be made available on request.

References

[1] M.M. Hossain Bhuiyan, Z. Siddique, Hydrogen as an alternative fuel: a comprehensive review of challenges and opportunities in production, storage, and transportation, Int. J. Hydrog. Energy 102 (2025) 1026–1044.
[2] R. Li, J. Luan, Y. Zhang, L. Jiang, H. Yan, Q. Chi, Z. Yan, A review of efficient photocatalytic water splitting for hydrogen production, Renew. Sustain. Energy Rev. 206 (2024) 114863.
[3] X. Tao, Y. Zhao, S. Wang, C. Li, R. Li, Recent advances and perspectives for solar-driven water splitting using particulate photocatalysts, Chem. Soc. Rev. 51 (9) (2022) 3561–3608.
[4] T.T. Le, P. Sharma, B.J. Bora, V.D. Tran, T.H. Truong, H.C. Le, P.Q.P. Nguyen, Fueling the future: a comprehensive review of hydrogen energy systems and their challenges, Int. J. Hydrog. Energy 54 (2024) 791–816.
[5] R.-P. Ye, J. Ding, W. Gong, M.D. Argyle, Q. Zhong, Y. Wang, C.K. Russell, Z. Xu, A. G. Russell, Q. Li, M. Fan, Y.-G. Yao, CO2 hydrogenation to high-value products via heterogeneous catalysis, Nat. Commun. 10 (2019) 5698.
[6] Y. Yamada, T. Miyahigashi, K. Ohkubo, S. Fukuzumi, Photocatalytic hydrogen evolution from carbon-neutral oxalate with 2-phenyl-4-(1-naphthyl)quinolinium ion and metal nanoparticles, Phys. Chem. Chem. Phys. 14 (2012) 10564–10571.
[7] Y. Lei, X. Sala, J. García-Antón, J. Muñoz, Versatile organometallic synthesis of 0D/2D metal@germanane nanoarchitectonics for electrochemical energy conversion applications, Small Methods 9 (2025) 2400854.
[8] G. Martí, L. Mallón, N. Romero, L. Francàs, R. Bofill, K. Philippot, J. García-Antón, X. Sala, Surface-functionalized nanoparticles as catalysts for artificial photosynthesis, Adv. Energy Mater. 13 (2023) 2300282.
[9] J. Creus, S. Drouet, S. Suriñach, P. Lecante, V. Collière, R. Poteau, K. Philippot, J. García-Antón, X. Sala, Ligand-capped Ru nanoparticles as efficient electrocatalyst for the hydrogen evolution reaction, ACS Catal. 8 (2018) 11094–11102.
[10] Y. Li, X. Liu, J. Xu, S. Chen, Ruthenium-based electrocatalysts for hydrogen evolution reaction: from nanoparticles to single atoms, Small 20 (2024) 2402846.
[11] J. Creus, J. De Tovar, N. Romero, J. García-Antón, K. Philippot, R. Bofill, X. Sala, Ruthenium nanoparticles for catalytic water splitting, ChemSusChem 12 (2019) 2493–2514.
[12] S. Fukuzumi, Y. Yamada, Catalytic activity of metal-based nanoparticles for photocatalytic water oxidation and reduction, J. Mater. Chem. 22 (2012) 24284–24296.
[13] N. Romero, R.B. Guerra, L. Gil, S. Drouet, I. Salmeron-Sànchez, O. Illa, K. Philippot, M. Natali, J. García-Antón, X. Sala, TiO_2-mediated visible-light-driven hydrogen evolution by ligand-capped Ru nanoparticles, Sustain. Energy Fuels 4 (2020) 4170–4178.
[14] Y. Yamada, K. Yano, S. Fukuzumi, Photocatalytic hydrogen evolution using 9-phenyl-10-methyl-acridinium ion derivatives as efficient electron mediators and Ru-based catalysts, Aust. J. Chem. 65 (2012) 1573–1581.
[15] V. Nikolaou, E. Agapaki, E. Nikoloudakis, K. Achilleos, K. Ladomenou, G. Charalambidis, E. Triantafyllou, A.G. Coutsolelos, Highly efficient light-driven hydrogen evolution utilizing porphyrin-based nanoparticles, Chem. Commun. 59 (2023) 11256–11259.
[16] M. Huber-Gedert, M. Nowakowski, A. Kertmen, L. Burkhardt, N. Lindner, R. Schoch, R. Herbst-Irmer, A. Neuba, L. Schmitz, T. Choi, J. Kubicki, W. Gawelda, M. Bauer, Fundamental characterization, photophysics and photocatalysis of a base metal iron(II)-cobalt(III) dyad, Chem. Eur. J. 27 (2021) 9905–9918.
[17] C. Kasahara, K. Rediger, M. Micheel, P. Liebing, S. Gräfe, S. Kupfer, M. Wächtler, W. Weigand, Molecular dyad vs multi-component approach-photocatalytic hydrogen evolution by combining oligothiophene photosensitizers with [FeFe]-hydrogenase mimics, ChemCatChem 16 (11) (2024) e202400247.
[18] M. Rupp, T. Auvray, E. Rousset, G.M. Mercier, V. Marvaud, D.G. Kurth, G.S. Hanan, Photocatalytic hydrogen evolution driven by a heteroleptic ruthenium(II) bis (terpyridine) complex, Inorg. Chem. 58 (2019) 9127–9134.
[19] C. Lentz, O. Schott, T. Auvray, G.S. Hanan, B. Elias, Design and photophysical studies of iridium(iii)–cobalt(iii) dyads and their application for dihydrogen photo-evolution, Dalton Trans. 48 (41) (2019) 15567–15576.
[20] V. Artero, M. Fontecave, Solar fuels generation and molecular systems: is it homogeneous or heterogeneous catalysis? Chem. Soc. Rev. 42 (2013) 2338–2356.
[21] V. Nikolaou, G. Charalambidis, G. Landrou, E. Nikoloudakis, A. Planchat, R. Tsalameni, K. Junghans, A. Kahnt, F. Odobel, A.G. Coutsolelos, Antenna effect in BODIPY-(Zn)porphyrin entities promotes H_2 evolution in dye-sensitized photocatalytic systems, ACS Appl. Energy Mater. 4 (9) (2021) 10042–10049.
[22] Y. Yamada, T. Miyahigashi, H. Kotani, K. Ohkubo, S. Fukuzumi, Photocatalytic hydrogen evolution under highly basic conditions by using Ru nanoparticles and 2-phenyl-4-(1-naphthyl)quinolinium ion, J. Am. Chem. Soc. 133 (2011) 16136–16145.
[23] M. Watanabe, Dye-sensitized photocatalyst for effective water splitting catalyst, Sci. Technol. Adv. Mater. 18 (2017) 705–723.
[24] T. Baron, D. Romito, L. Corne, B. Andrin, Y. Pellegrin, F. Odobel, Dye-sensitized photocatalytic hydrogen production promoted by near-infrared pyrrolopyrrole cyanine sensitizers, ACS Appl. Energy Mater. 7 (2024) 4690–4697.
[25] E. Bae, W. Choi, Effect of the anchoring group (carboxylate vs phosphonate) in Ru-complex-sensitized TiO $_2$ on hydrogen production under visible light, J. Phys. Chem. B 110 (2006) 14792–14799.
[26] A. Kobayashi, S. Watanabe, M. Yoshida, M. Kato, Importance of the molecular orientation of an iridium(III)-heteroleptic photosensitizer immobilized on TiO_2 nanoparticles, ACS Appl. Energy Mater. 1 (2018) 2882–2890.
[27] G. Li, M.F. Mark, H. Lv, D.W. McCamant, R. Eisenberg, Rhodamine-platinum diimine dithiolate complex dyads as efficient and robust photosensitizers for light-driven aqueous proton reduction to hydrogen, J. Am. Chem. Soc. 140 (2018) 2575–2586.
[28] K. Maeda, G. Sahara, M. Eguchi, O. Ishitani, Hybrids of a ruthenium(II) polypyridyl complex and a metal oxide nanosheet for dye-sensitized hydrogen evolution with visible light: effects of the energy structure on photocatalytic activity, ACS Catal. 5 (2015) 1700–1707.
[29] M.R. Axet, K. Philippot, Catalysis with colloidal ruthenium nanoparticles, Chem. Rev. 120 (2020) 1085–1145.
[30] N. Romero, D.A. Fenoll, L. Gil, S. Campos, J. Creus, G. Martí, J. Heras-Domingo, V. Collière, C.A. Mesa, S. Giménez, L. Francàs, L. Rodríguez-Santiago, X. Solans-Monfort, M. Sodupe, R. Bofill, K. Philippot, J. García-Antón, X. Sala, Ru-based nanoparticles supported on carbon nanotubes for electrocatalytic hydrogen evolution: structural and electronic effects, Inorg. Chem. Front. 10 (2023) 5885–5896.
[31] L. Mallón, J. Navarro-Ruiz, C. Cerezo-Navarrete, N. Romero, I. Del Rosal, J. García-Antón, R. Bofill, L.M. Martínez-Prieto, K. Philippot, R. Poteau, X. Sala, Effect of nitrogen and phosphorus doping of reduced graphene oxide in the hydrogen evolution catalytic activity of supported Ru nanoparticles, ACS Appl. Mater. Interfaces 17 (2025) 6198–6210.
[32] E. Rousset, I. Ciofini, V. Marvaud, G.S. Hanan, Facile one-pot synthesis of ruthenium(II) quaterpyridine-based photosensitizers for photocatalyzed hydrogen production, Inorg. Chem. 56 (2017) 9515–9524.
[33] E. Rousset, D. Chartrand, I. Ciofini, V. Marvaud, G.S. Hanan, Red-light-driven photocatalytic hydrogen evolution using a ruthenium quaterpyridine complex, Chem. Commun. 51 (2015) 9261–9264.
[34] B.P. Sullivan, D.J. Salmon, T.J. Meyer, Mixed phosphine 2,2'-bipyridine complexes of ruthenium, Inorg. Chem. 17 (1978) 3334–3341.
[35] D. Rota Martir, M. Averardi, D. Escudero, D. Jacquemin, E. Zysman-Colman, Photoinduced electron transfer in supramolecular ruthenium–porphyrin assemblies, Dalton Trans. 46 (2017) 2255–2262.
[36] D.R. Baer, K. Artyushkova, H. Cohen, C.D. Easton, M. Engelhard, T.R. Gengenbach, G. Greczynski, P. Mack, D.J. Morgan, A. Roberts, XPS guide: charge neutralization and binding energy referencing for insulating samples, J. Vac. Sci. Technol. A 38 (2020) 031204.

[37] N. Fairley, V. Fernandez, M. Richard-Plouet, C. Guillot-Deudon, J. Walton, E. Smith, D. Flahaut, M. Greiner, M. Biesinger, S. Tougaard, D. Morgan, J. Baltrusaitis, Systematic and collaborative approach to problem solving using X-ray photoelectron spectroscopy, Appl. Surf. Sci. Adv. 5 (2021) 100112.
[38] N. Klippel, G. Jung, G. Kickelbick, Hybrid inorganic-organic fluorescent silica nanoparticles—influence of dye binding modes on dye leaching, J. Sol-Gel Sci. Technol. 107 (2023) 2–19.
[39] E. Martín Morales, Y. Coppel, P. Lecante, I. del Rosal, R. Poteau, J. Esvan, P. Sutra, K. Philippot, A. Igau, When organophosphorus ruthenium complexes covalently bind to ruthenium nanoparticles to form nanoscale hybrid materials, Chem. Commun. 56 (2020) 4059–4062.
[40] A.M. López-Vinasco, L.M. Martínez-Prieto, J.M. Asensio, P. Lecante, B. Chaudret, J. Cámpora, P.W.N.M. Van Leeuwen, Novel nickel nanoparticles stabilized by imidazolium-amidinate ligands for selective hydrogenation of alkynes, Catal. Sci. Technol. 10 (2020) 342–350.
[41] D.J. Morgan, Resolving ruthenium: XPS studies of common ruthenium materials, Surf. Interface Anal. 47 (2015) 1072–1079.
[42] Y. Pellegrin, F. Odobel, Sacrificial electron donor reagents for solar fuel production, C. R. Chim. 20 (2016) 283–295.
[43] C.K. Prier, D.A. Rankic, D.W.C. MacMillan, Visible Light photoredox catalysis with transition metal complexes: applications in organic synthesis, Chem. Rev. 113 (2013) 5322–5363.
[44] Y. Luo, Z.-Y. Xu, H. Wang, X.-W. Sun, Z.-T. Li, D.-W. Zhang, Porous $Ru(Bpy)_3^{2+}$-linked polymers for recyclable photocatalysis of enantioselective alkylation of aldehydes, ACS Macro Lett. 9 (1) (2020) 90–95.
[45] J.-L. Wang, C. Wang, K.E. deKrafft, W. Lin, Cross-linked polymers with exceptionally high $Ru(Bipy)_3^{2+}$ loadings for efficient heterogeneous photocatalysis, ACS Catal. 2 (3) (2012) 417–424.
[46] B.F. DiSalle, S. Bernhard, Orchestrated photocatalytic water reduction using surface-adsorbing iridium photosensitizers, J. Am. Chem. Soc. 133 (31) (2011) 11819–11821.
[47] M.R. Norris, J.J. Concepcion, C.R.K. Glasson, Z. Fang, A.M. Lapides, D.L. Ashford, J.L. Templeton, T.J. Meyer, Synthesis of phosphonic acid derivatized bipyridine ligands and their ruthenium complexes, Inorg. Chem. 52 (21) (2013) 12492–12501.